Review of Scientific Instruments

RESEARCH ARTICLE | SEPTEMBER 20 2023

The Harpers THMC flow bench: A triaxial multi-reactor setup for the investigation of long-term coupled thermo-hydro-mechanical-chemical fluid-rock interaction

Nick Harpers ; Ming Wen ; Paul Miller; Suzanne Hangx ; Andreas Busch

Rev. Sci. Instrum. 94, 095112 (2023)
https://doi.org/10.1063/5.0160906

Review of Scientific Instruments ARTICLE pubs.aip.org/aip/rsi

The Harpers THMC flow bench: A triaxial multi-reactor setup for the investigation of long-term coupled thermo-hydro-mechanical-chemical fluid-rock interaction

Cite as: Rev. Sci. Instrum. 94, 095112 (2023); doi: 10.1063/5.0160906
Submitted: 6 June 2023 • Accepted: 21 August 2023 •
Published Online: 20 September 2023

Nick Harpers,[1,a)] Ming Wen,[1] Paul Miller,[1] Suzanne Hangx,[2] and Andreas Busch[1]

AFFILIATIONS

[1] GeoEnergy Group, The Lyell Centre, Heriot-Watt-University, Edinburgh EH14 4AS, Scotland, United Kingdom
[2] Experimental Rock Deformation Group, Department of Earth Sciences, Utrecht University, Utrecht 3584 CB, Netherlands

[a)] **Author to whom correspondence may be addressed:** nh57@hw.ac.uk

ABSTRACT

The scientific analysis and interpretation of coupled thermo-hydro-mechanical-chemical (THMC) processes in rocks requires complex and diverse instrumentation. In this study, we introduce the "Harpers THMC Flow Bench," a multi-cell, flow-through reactor system that allows long-term testing on rock plugs and powdered samples. The setup consists of four small triaxial cells that can hold confining and pore pressure of up to 20 MPa and an axial load of up to 300 MPa. Axial deformation of the samples is measured with linear variable differential transducers. The cells can be heated to 90 °C, and effluents (gas, water, and brine) can be sampled for compositional analysis. An additional Hastelloy-autoclave enables fluid mixing and saturation with gas prior to injection into the samples. Each cell can be operated individually, allowing independent experiments over long testing periods. The sample holders were designed such that they are transparent for X-rays during X-ray computer tomography, minimizing sample handling effects on the imaging results. To demonstrate examples of the capabilities of the flow bench, we present case studies on Carnmenellis granite (Cornwall, UK) and Castlegate sandstone (Utah, USA) samples. Permeability measurements are shown using fractured granite undergoing periodic loading of effective pressure. To demonstrate chemical measurement capabilities, we used deionized water to leach elements from granite powders. We then analyzed effluent compositions using inductively coupled plasma optical emission spectroscopy. Finally, we conducted a strength test and a cyclic differential stress test on sandstone to demonstrate the mechanical testing capabilities of the setup.

I. INTRODUCTION

Carbon capture and geological storage, geological storage of hydrogen, geothermal energy production, or radioactive waste disposal are examples of modern technologies and concepts to tackle the problems of energy transition and climate change in geological systems (Bui *et al.*, 2018; Chapman and Hooper, 2012; Goldstein *et al.*, 2011; and Tarkowski, 2019). Each of the technologies requires access to or engineering of geological host structures and will affect the local rock by changing *in situ* conditions such as stress state, temperature, geochemistry, and pressure. For de-risking the utilization of such geoenergy reservoirs, it is key to identify and understand the coupled processes occurring due to human activities in the subsurface. The injection of new fluids can lead to thermal changes, density variations, and changes in the state of stress. In turn, these changes can impact hydraulic conductivity,

deformation behavior, and chemical interactions between the host rock and injected fluid, as studied extensively over the years (Hangx *et al.*, 2015; Hangx *et al.*, 2010; Heinemann *et al.*, 2021; Kim and Santamarina, 2016; Nermoen *et al.*, 2015; and Phillips *et al.*, 2021). Since their coupling is complex, the more factors considered simultaneously, the harder it gets to distinguish the importance of each individual component. In nature, all aspects act at once, and decoupling or ignoring processes are necessary simplifications for interpreting field data. In the lab, artificial systems can be created that allow for the isolation of individual components to focus on understanding single aspects or couplings.

Commonly used setups to investigate (coupled) rock properties in the laboratory are triaxial deformation apparatus [e.g., Faulkner and Armitage (2013) and Yasuhara (2018)], autoclaves or batch reactors [e.g., Lo Ré *et al.* (2014) and Savage *et al.* (1993)], and permeameters [e.g., Cheng and Milsch (2020) and Nara *et al.* (2018)]. Triaxial deformation machines, focusing on sample deformation at elevated pressure and temperature, often allow simultaneous flow measurements along a sample. However, due to their complex and expensive design, pore fluid chemistry is often limited to water [e.g., Faoro *et al.* (2016), Grimm Lima *et al.* (2019), and Hangx and Brantut (2019)], restricting their use for geochemical applications. Chemical fluid-rock interaction experiments are mostly conducted in autoclaves or batch reactors. As such, fluids can be reacted with rocks at elevated pressure and temperature, and the resulting fluid and rock compositions can be analyzed [e.g., Drüppel *et al.* (2020), Lo Ré *et al.* (2014), and Savage *et al.* (1993)]. These autoclaves typically do not allow for sample deformation or permeametry. For permeameters, focused on measuring the hydraulic properties of the rocks, temperature and pressure can be controlled, and different fluids like water or N_2 can be used to measure absolute permeability [e.g., Boulin *et al.* (2012) and Forbes Inskip *et al.* (2022)] or even to study multi-phase flow [e.g., Krevor *et al.* (2012)]. In recent years, many of the aforementioned types of equipment have been expanded upon to accommodate the research needed to investigate THMC processes. Kamali-Asl *et al.* (2018) sampled and analyzed effluents that passed through rock fractures at high pressure and temperature within triaxial loading conditions to investigate how

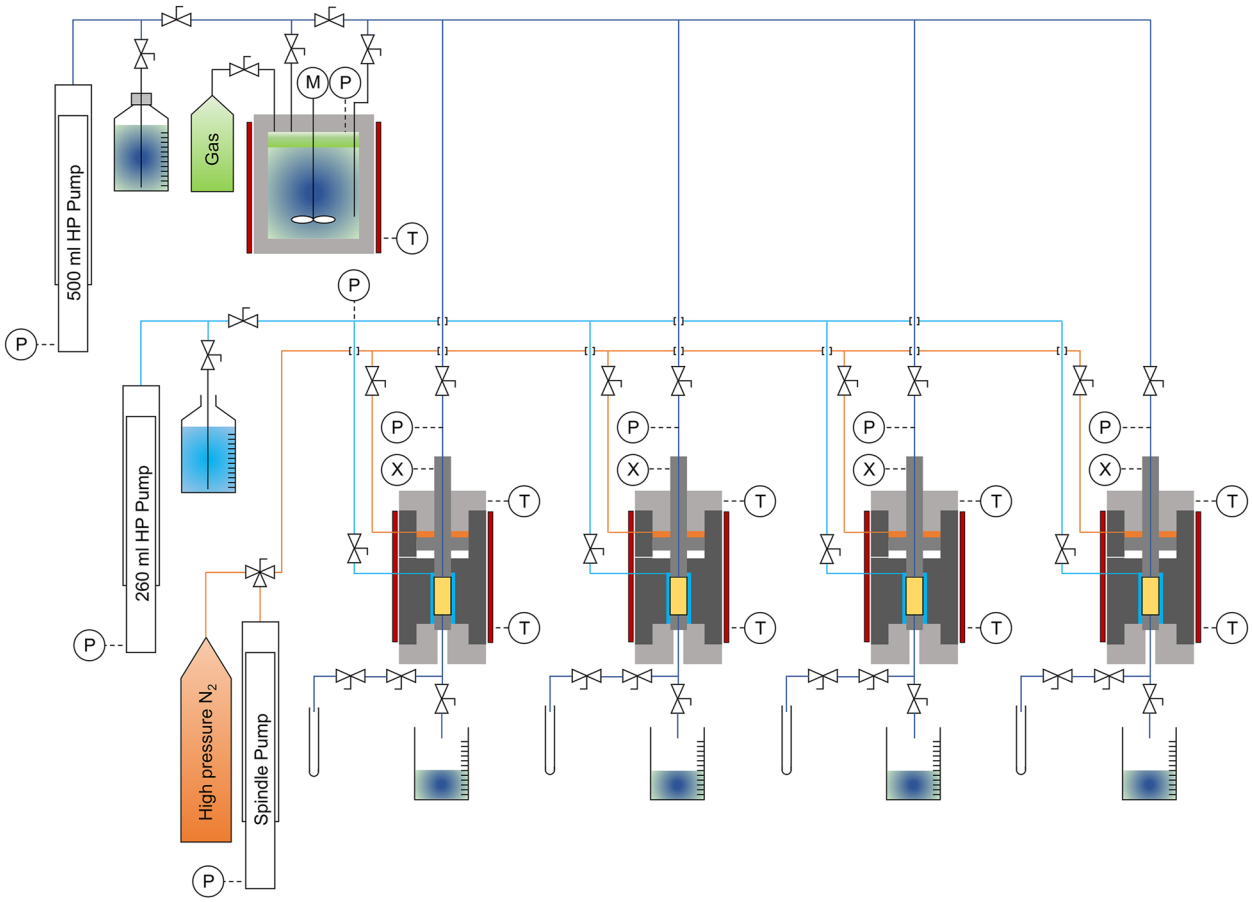

FIG. 1. Schematic of the Harpers THMC Flow Bench in parallel vessel configuration with each pressure system fed from one pump. Different sensors are represented by circles: T for thermometers, P for pressure transducers, and X for LVDTs. M indicates an adjustable high-pressure stirrer. Capillaries are color coded to indicate fluid: orange represents working gas (e.g., nitrogen), light blue deionized water, dark blue water, brines, and gas saturated fluids.

pressure solution or subcritical fracture propagation (stress corrosion cracking) affected fracture hydraulics. Cheng and Milsch (2020) used a hydrostatic permeameter to flow deionized water through a fracture in quartz sandstone and observe pressure solution effects on permeability.

However, the response of rock to changes in stress, pressure, temperature, and chemical environment tends to be highly time-dependent [e.g., Schimmel *et al.* (2019)]. Equipment availability and system tightness make long-term experiments, beyond the timescale of a few days or weeks, very challenging. While some processes in rocks can act fast (e.g., catastrophic fracturing), others can be slow (e.g., creep, chemical, or stress-induced dissolution) and may require long-term observation over days, weeks, or months to be analyzed. Therefore, real long-term experiments are rare, and long-term effects and coupled THMC processes are still only partially understood. The longest experiments we know of were performed on chalk by Hellmann *et al.* (2002) for almost 700 days and by Nermoen *et al.* (2015) for 1072 days, where the rocks interacted with fluids under chemically closed (no flow) and chemically open (flow) conditions to investigate creep and pressure solution effects within triaxial cells.

In this paper, we present the "Harpers THMC Flow Bench" (HFB), which is a multi-sample setup designed to investigate complex coupled THMC processes in rocks by combining four small heatable triaxial cells with the capability to monitor permeability, axial deformation, and chemical fluid-rock interaction. The system allows the injection of brines at pressure and temperature into the cells that hold porous or fractured rock samples over long periods of time. Furthermore, an axial stress intensifier allows the application of up to 300 MPa of axial load for mechanical testing. In this work, we demonstrate the setups' functionality on fractured granite, intact porous sandstone, and granite gouge.

II. SETUP DESIGN

A. Reactor cells and sample holders

The design consists of four equally build, serially placed, small-scale high-pressure cells (Fig. 1), allowing for small rock samples (10 mm in diameter by 20 mm in length) to be placed under *in situ* stress conditions through independent application of confining pressure and axial stress in the presence of high-pressure and high temperature water and brine. Having four equally built cells enables parallel testing with only small adjustments to testing parameters. Monitoring differences between tests running in parallel allows for a more detailed investigation of small parameter changes and an understanding of the effects of changes in testing parameters or strategy. As THMC experimentation depends on a high number of parameters, having more cells allows covering more parameters in parallel. Furthermore, having multiple cells also enables long-term testing, as a single cell can be occupied while the others are used for other tests. Each of the cells is made of stainless steel and consists of a pressure vessel containing the sample. Hydrogenated nitrile rubber (HNBR) and fluoroelastomer (FKM or Viton®) O-rings are used on all static and dynamic seals. Overall, the four parallel cells will be controlled by three separate systems to control confining pressure (P_c), axial stress (σ_{ax}), and pore fluid pressure (P_p). Note that when running cells in serial configuration (Fig. 1), none of these parameters can be controlled separately for each cell. However, valves surrounding each cell allow isolation of individual cells from the

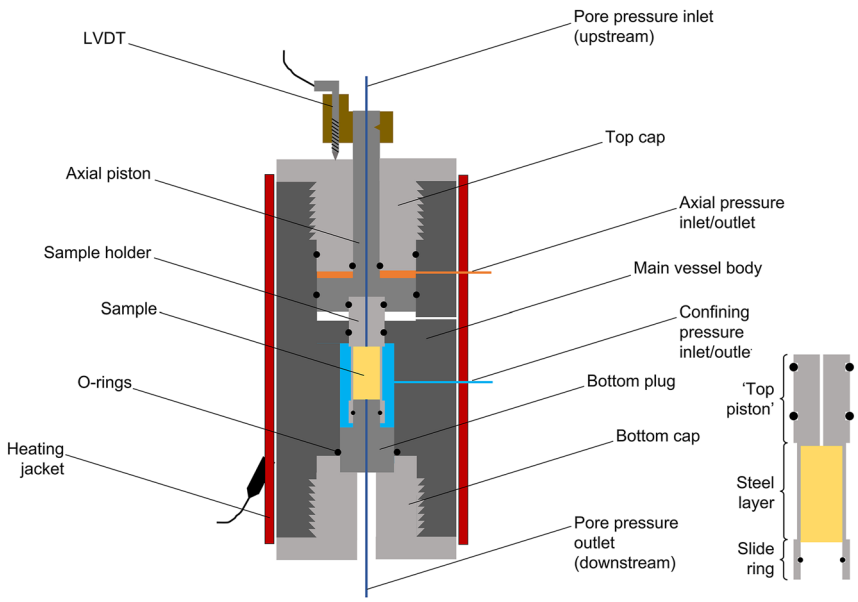

FIG. 2. Single cell design. A LVDT is fitted to the top piston to monitor the axial deformation of the sample by measuring the displacement of the piston against the top cap. A sample holder is shown on the bottom right. Samples are fitted to sit within the thin steel layer, allowing radial stresses to be transferred through the compressed steel onto the sample material.

main lines and, therefore, separate operation. In this state, four individual batch-type experiments can be established, and mechanical properties can be measured individually. In total, 13 pressure relief valves are fitted to the three systems to ensure safe operation below the maximum pressure of 20 MPa.

To ensure constant pressure or flow rate control, two high pressure syringe pumps (Teledyne ISCO, USA) individually control confining pressure (up to 20 MPa range, 260 ml volume) and pore pressure (up to 20 MPa range, 500 ml volume). The pumps allow the recording of pressure, pump volume, and flow rate. Further pressures are measured using high precision pressure transducers (Keller, Switzerland; pressures up to 20 MPa; error 0.1% of the full-scale pressure value) connected to the lines around each cell. An axial load is applied to the sample by means of a movable top piston (Fig. 2). The piston is controlled by injecting pressurized N_2 into a chamber located at the top of the pressure vessel, which can be monitored using a pressure gauge and an additional pressure transducer. The gas pressure is controlled through a spindle pump, and the system allows up to 20 MPa of gas pressure. The gas pressure creates a load on the piston seat and transfers an axial stress onto the sample. Due to the difference in area between the seat and the sample contact, there will be a stress amplification between the applied pressure and the stress on the sample (amplification factor ~15; axial stress up to 300 MPa).

A heating collar is fitted around the vessel and allows the application of temperatures up to 90 °C (maximum to avoid the formation of steam in the pore pressure system). Temperatures are monitored with resistance temperature detectors (RTD, accuracy ±[0.3 °C + 0.005 T]) fixed to the top cap and heating jacket of each cell. Both the top and bottom pistons are equipped with a central bore. Pore fluid, (gas-saturated) brine, can be introduced into the samples through these inlets. The fluid can either be prepared before the experiment and filled into the pore pressure syringe pump or mixed in a separate Hastelloy autoclave at pressure and temperature prior to injection into the system. Hastelloy is a nickel-based metal alloy that is more corrosion resistant than stainless steel and, therefore, preferred in many chemical applications. The autoclave can also be fed from an additional gas bottle, which allows fluid saturation with gases like carbon dioxide or hydrogen. As the current tubing system of the cells is constructed of stainless steel (same as the reactor cells), the passing of acid brine may lead to corrosion. The artificial brine can be pressurized using the syringe pump, and pore pressure is monitored using pressure gauges and pressure transducers in each cell. Each cell is equipped with a set of valves to isolate the cell from the system and allow pore fluid to be extracted from the sample for analysis.

For the sample assembly, a special core holder was designed to accommodate the small sample size of 10 mm in diameter by 20 mm in length. The holder is made from one solid piece of steel and consists of three sections. A 0.064 mm thin steel layer surrounding the sample connects a solid top piston, containing a central bore and two (dynamic) O-ring seals, with a slide ring at the bottom (see Fig. 2). The steel layer is thin enough to allow x-ray computer tomography (CT) scanning of the sample before, during, or after the experiment. It is compressed against the sample under confining pressure, which then transfers the radial stress onto the sample. Depending on the sample diameter, the steel might wrinkle when compressed around the sample. To avoid fluid channeling through these wrinkles around the sample, polytetrafluoroethylene (PTFE) tape surrounds the rock and seals the space between the sample and steel sleeve. When assembling, the "top piston" of the sample assembly is inserted into the cell against the loading top piston. The bottom piston, also with a central bore, is fitted into the bottom slide ring and sealed by an O-ring (static seal). Under axial load, the sample holder is moved onto the bottom piston, which then applies load to the sample and can cause axial deformation. Axial deformation is monitored with a LVDT (linear variable differential transducer; ±2 mm range; 4 μm accuracy), externally measuring the position of

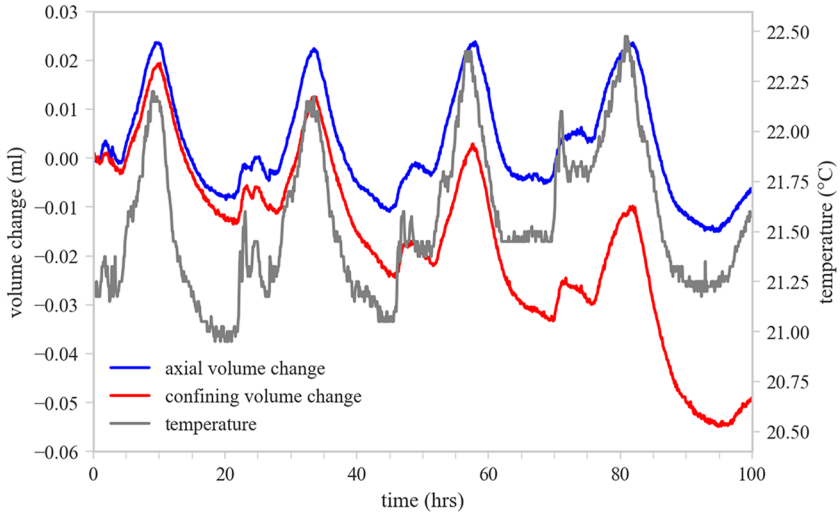

FIG. 3. Leak rates for the axial and confining volume systems, as measured for cell 3. Note the diurnal fluctuations in temperature, which cause fluctuations in the various system volumes.

TABLE I. Summary of the leak rates measured for cells 2 to 4, measured during a single moment in time after assembly. "Positive" leak rates are most likely an effect of temperature fluctuations (see Fig. 3).

Leak rate	Axial volume (μl/h)	Confining volume (μl/h)
Cell 2	−0.285	−4.00
Cell 3	+0.017	−0.381
Cell 4	−0.190	−0.767

the top piston with respect to the pressure vessel. The stainless steel has been proven to be little to non-reactive with brine under specific restrictions, ensuring the integrity of the sample assembly over the time span of the experiments. Note that the O-ring seals located within the top piston might pose issues with respect to friction, while no issues are expected with the bottom piston O-rings.

Samples can either be rock cylinders of 10 mm diameter by 20 mm length or rock powders/sand packs, depending on the application and specific goals of the experiments. If additional porous plates are needed (e.g., for equal fluid dispersion over a fractured sample), their thickness needs to be considered and the sample length reduced accordingly.

B. System limitations

We conducted an extensive testing phase to determine the limits of the setup. In addition to the general limits to the applicable conditions (T_{max} = 90 °C, $P_{c_{max}}$ = 20 MPa, $P_{P_{max}}$ = 20 MPa, $\sigma_{a_{max}}$ = 300 MPa), possible effects of the setup on the different measurements were investigated. The tubing in the system as well as the sample holders are made from stainless steel, which limits the composition of the used brines. The fluids should not corrode the steel, allowing alkaline compositions but restricting the use of strong acids or fluids high in chloride. For more corrosive fluids, the steel sample holders can be switched out with Hastelloy holders, but in long-term experiments, tubing and connections should be monitored regularly for leaks.

The individual leak rates of cells 2, 3, and 4 were measured. For each measurement, the selected cell was separated from the remaining three cells by closing the valves between the different cells. As a result, only the selected cell was in direct communication with the axial, confining, and pore fluid pressure pumps. After applying a fixed confining pressure to the cell (P_c = 10 MPa), it was left under pressure for several days while measuring the volumetric changes in the axial, confining, and pore pressure systems. These measurements give an indication of the volumetric leak rate of the different pressure systems. As seen in Fig. 3, temperature fluctuations have a significant effect on volumetric measurements as a result of the expansion and contraction of fluid in response to temperature shifts, such as day and night cycles. It is possible for temperature fluctuations to overprint any actual leakages, as seen for the confining and pore volumes.

Overall, the leak rates of the various cells are reasonably small. Small pressure losses are expected due to the large number of connections in the setup and across the various taps. It is technically only feasible to reduce leakage further by soldering all connections, which may pose issues when pieces of equipment need to be replaced. A summary of the leak rates measured for cells 2–4 is shown in Table I. "Positive" leak rates are most likely an effect of temperature fluctuations. It should be noted that the measured leak rates are only a snapshot in time, as they may change when cells are being disassembled and reassembled. However, when the assembly is properly maintained, leak rates are up to several microliters per hour, meaning

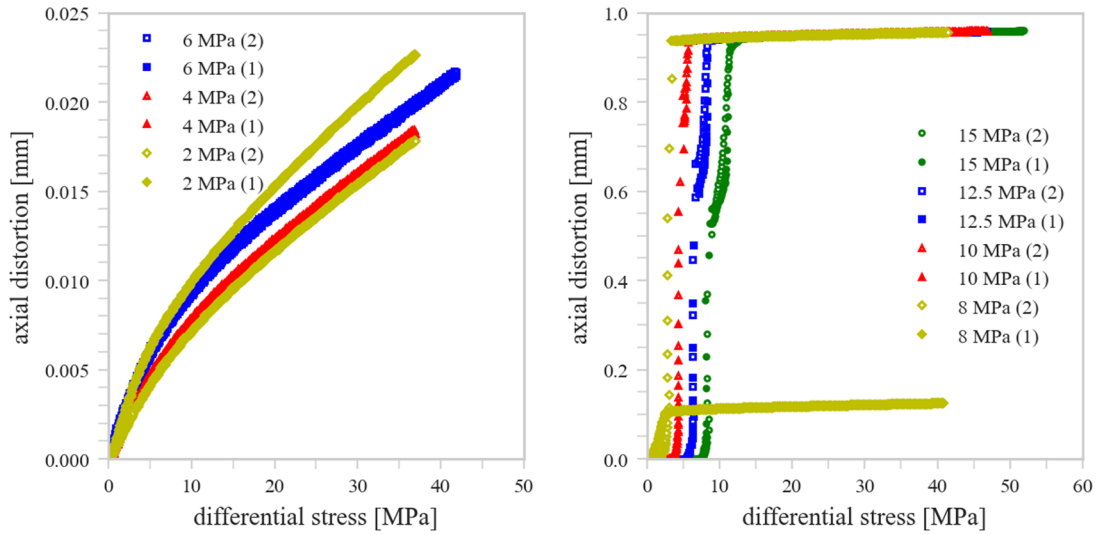

FIG. 4. Axial distortion vs differential stress for stiffness calibration measurements performed for cell 3 during the loading cycles (unloading cycles not shown). Note that there are two clear regimes: (1) up to 6 MPa confining pressure (left) and (2) at >6 MPa confining pressure (right). All measurements are corrected for the elastic deformation of the aluminum dummy.

TABLE II. Functions describing apparatus distortion in displacement measurements for the loading and unloading parts of the experiment.

LOADING SEQUENCE		
P_c (MPa)	Stiffness correction (mm)	Volumetric distortion (ml)
	Regime 1: Polynomial functions for $(\sigma_1 - \sigma_3) \le 20$ MPa	
$0 < P_c \le 2$	$dx = 3.71 \times 10^{-11}(\sigma_1 - \sigma_3)^6 - 3.37 \times 10^{-9}(\sigma_1 - \sigma_3)^5 + 1.27 \times 10^{-7}(\sigma_1 - \sigma_3)^4 - 1.67 \times 10^{-6}(\sigma_1 - \sigma_3)^3 - 1.17 \times 10^{-5}(\sigma_1 - \sigma_3)^2 + 9.09 \times 10^{-4}(\sigma_1 - \sigma_3)$	$dV = -4.19 \times 10^{-6}(\sigma_1 - \sigma_3)^2 + 4.94 \times 10^{-4}(\sigma_1 - \sigma_3)$
$2 < P_c \le 4$	$dx = 2.93 \times 10^{-11}(\sigma_1 - \sigma_3)^6 - 3.10 \times 10^{-9}(\sigma_1 - \sigma_3)^5 + 1.11 \times 10^{-7}(\sigma_1 - \sigma_3)^4 - 1.10 \times 10^{-6}(\sigma_1 - \sigma_3)^3 - 2.52 \times 10^{-5}(\sigma_1 - \sigma_3)^2 + 1.07 \times 10^{-3}(\sigma_1 - \sigma_3)$	$dV = -2.13 \times 10^{-6}(\sigma_1 - \sigma_3)^2 + 2.79 \times 10^{-4}(\sigma_1 - \sigma_3)$
$4 < P_c \le 6$	$dx = -7.99 \times 10^{-12}(\sigma_1 - \sigma_3)^6 + 1.48 \times 10^{-9}(\sigma_1 - \sigma_3)^5 - 1.11 \times 10^{-7}(\sigma_1 - \sigma_3)^4 + 4.35 \times 10^{-6}(\sigma_1 - \sigma_3)^3 - 9.75 \times 10^{-5}(\sigma_1 - \sigma_3)^2 + 1.58 \times 10^{-3}(\sigma_1 - \sigma_3)$	$dV = -1.71 \times 10^{-7}(\sigma_1 - \sigma_3)^2 + 1.11 \times 10^{-4}(\sigma_1 - \sigma_3)$
	Regime 1: Linear functions for $(\sigma_1 - \sigma_3) > 20$ MPa	
$0 < P_c \le 6$	$dx = (-6.84 \times 10^{-6}\, P_c + 4.09 \times 10^{-4})\,(\sigma_1 - \sigma_3) + 3.73 \times 10^{-3}$	$dV = (-4.89 \times 10^{-5}\, P_c + 3.91 \times 10^{-4})\,(\sigma_1 - \sigma_3) + 2.34 \times 10^{-3}$
	Regime 2: Polynomial functions for $(\sigma_1 - \sigma_3) \le 20$ MPa	
$P_c > 6$	$dx = -2.24 \times 10^{-11}(\sigma_1 - \sigma_3)^6 + 3.06 \times 10^{-9}(\sigma_1 - \sigma_3)^5 - 1.69 \times 10^{-7}(\sigma_1 - \sigma_3)^4 + 4.90 \times 10^{-6}(\sigma_1 - \sigma_3)^3 - 8.19 \times 10^{-5}(\sigma_1 - \sigma_3)^2 + 1.15 \times 10^{-3}(\sigma_1 - \sigma_3)$	$dV = -2.11 \times 10^{-6}(\sigma_1 - \sigma_3)^2 + 2.74 \times 10^{-4}(\sigma_1 - \sigma_3)$
	Regime 2: Linear functions for $(\sigma_1 - \sigma_3) > 20$ MPa	
$P_c > 6$	$dx = 3.57 \times 10^{-4}\,(\sigma_1 - \sigma_3) + 3.69 \times 10^{-3}$	$dV = 1.72 \times 10^{-4}\,(\sigma_1 - \sigma_3) + 1.20 \times 10^{-3}$
UNLOADING SEQUENCE		
P_c (MPa)	Stiffness correction (mm)	Volumetric distortion (ml)
	Regime 1: Polynomial functions for $(\sigma_1 - \sigma_3) \le 20$ MPa	
$0 < P_c \le 2$	$dx = -5.32 \times 10^{-11}(\sigma_1 - \sigma_3)^6 + 6.50 \times 10^{-9}(\sigma_1 - \sigma_3)^5 - 3.18 \times 10^{-7}(\sigma_1 - \sigma_3)^4 + 8.06 \times 10^{-6}(\sigma_1 - \sigma_3)^3 - 1.17 \times 10^{-4}(\sigma_1 - \sigma_3)^2 + 1.40 \times 10^{-3}(\sigma_1 - \sigma_3)$	$dV = 9.42 \times 10^{-7}(\sigma_1 - \sigma_3)^2 + 2.11 \times 10^{-4}(\sigma_1 - \sigma_3)$
$2 < P_c \le 4$	$dx = -6.17 \times 10^{-11}(\sigma_1 - \sigma_3)^6 + 7.72 \times 10^{-9}(\sigma_1 - \sigma_3)^5 - 3.87 \times 10^{-7}(\sigma_1 - \sigma_3)^4 + 9.99 \times 10^{-6}(\sigma_1 - \sigma_3)^3 - 1.46 \times 10^{-4}(\sigma_1 - \sigma_3)^2 + 1.61 \times 10^{-3}(\sigma_1 - \sigma_3)$	$dV = 1.82 \times 10^{-7}(\sigma_1 - \sigma_3)^2 + 1.47 \times 10^{-4}(\sigma_1 - \sigma_3)$
$4 < P_c \le 6$	$dx = -7.03 \times 10^{-12}(\sigma_1 - \sigma_3)^6 + 9.85 \times 10^{-9}(\sigma_1 - \sigma_3)^5 - 5.47 \times 10^{-7}(\sigma_1 - \sigma_3)^4 + 1.53 \times 10^{-5}(\sigma_1 - \sigma_3)^3 - 2.32 \times 10^{-4}(\sigma_1 - \sigma_3)^2 + 2.25 \times 10^{-3}(\sigma_1 - \sigma_3)$	$dV = -2.73 \times 10^{-7}(\sigma_1 - \sigma_3)^2 + 1.17 \times 10^{-4}(\sigma_1 - \sigma_3)$
	Regime 1: Linear functions for $(\sigma_1 - \sigma_3) > 20$ MPa	
$0 < P_c \le 6$	$dx = (-3.29 \times 10^{-6}\, P_c + 3.71 \times 10^{-4})\,(\sigma_1 - \sigma_3) + 3.73 \times 10^{-3}$	$dV = (-3.86 \times 10^{-5}\, P_c + 3.25 \times 10^{-4})\,(\sigma_1 - \sigma_3) + 2.34 \times 10^{-3}$
	Regime 2: Polynomial functions for $(\sigma_1 - \sigma_3) \le 20$ MPa	
$P_c > 6$	$dx = -9.59 \times 10^{-12}(\sigma_1 - \sigma_3)^6 + 1.25 \times 10^{-9}(\sigma_1 - \sigma_3)^5 - 6.64 \times 10^{-8}(\sigma_1 - \sigma_3)^4 + 1.89 \times 10^{-6}(\sigma_1 - \sigma_3)^3 - 3.26 \times 10^{-5}(\sigma_1 - \sigma_3)^2 + 6.70 \times 10^{-4}(\sigma_1 - \sigma_3)$	$dV = -2.73 \times 10^{-7}(\sigma_1 - \sigma_3)^2 + 1.17 \times 10^{-4}(\sigma_1 - \sigma_3)$
	Regime 2: Linear functions for $(\sigma_1 - \sigma_3) > 20$ MPa	
$P_c > 6$	$dx = 3.57 \times 10^{-4}\,(\sigma_1 - \sigma_3) + 3.69 \times 10^{-3}$	$dV = 1.72 \times 10^{-4}\,(\sigma_1 - \sigma_3) + 1.20 \times 10^{-3}$

leak rates of up to several tens of milliliters per year. This implies that the cells cannot be left isolated from the pressure system for an extended period of time, and frequent repressurization of the cells is advised.

A series of 14 control experiments were performed within the elastic regime to measure the stiffness of the cells with respect to axial displacement and volumetric changes. These measurements were only made for cell 3, as the remaining three cells were assumed to be nominally equal to cell 3. Furthermore, it was assumed that the set-up assembly and disassembly do not nominally change the apparatus stiffness and distortion. We used the high-pressure syringe pumps for radial and axial pressure, connected to cell 3, to accurately measure distortion.

During the calibrations, an aluminum dummy sample (E = 72 GPa, ν = 0.32) was placed in the core holder. Note that the dummy behaves elastically in the stress range used here. Knowing the elastic properties of this material, it was possible to determine the effect of the pressure cell on the axial and volumetric measurements. Each loading and unloading cycle was repeated twice to test for repeatability for radial pressures in the range of 2.0–15.0 MPa and axial stresses up to 55 MPa. Axial displacement was logged on a 5 s time scale using the LVDT. The data were corrected for the elastic distortion of the aluminum dummy sample. Axial distortion vs differential stress, i.e., axial stress minus radial pressure, was constructed to investigate the effect of apparatus stiffness (see Fig. 4 for all loading cycles; unloading cycles are not shown). It is clear from Fig. 4 that the apparatus needs to settle after assembly, which is observed in the different stress-displacement behavior during the first loading-unloading cycle.

From the data obtained, two regimes exist. At low confining pressure ($P_c \leq 6$ MPa—regime 1), up to differential stresses of ~20 MPa, distortion can be approached using polynomial functions for the different pressure regimes, while at higher pressure ($\sigma_1 - \sigma_3$), distortion can be approached by linear functions. At higher confining pressure ($P_c > 6$ MPa—regime 2), axial displacement can be approximated by a function independent of P_c, which is a polynomial function for $(\sigma_1 - \sigma_3) \leq 20$ MPa, and a linear function for $(\sigma_1 - \sigma_3) > 20$ MPa.

It should be noted that the axial displacement distortion of the apparatus shows clear trends with respect to confining pressure. Furthermore, comparing the loading and unloading parts of the data shows significant hysteresis. A summary of the different polynomials and linear functions to correct for apparatus distortion in displacement is shown in Table II, both for loading and unloading sequences, and graphs are shown in Fig. 5.

The observed transient step in the displacement at confining pressures of more than 6 MPa means that under these conditions, proper measurements cannot be made prior to the step unless one can properly correct for it. This is unlikely, as step-size shows no clear dependence. However, the onset of the step does show a systematic positive dependence on confining pressure and differential stress (Fig. 4). The dependence of stepping on confining pressure is an indication that this step is related to O-ring friction. Given the configuration of the pressure vessels, the stress amplifier built into the top piston (Fig. 2) could result in a significant friction effect, as is seen in our calibration measurements (Fig. 4). By taking the differential stress at the end of each step as a function of confining pressure, it is possible to delineate the stress fields for which measurements can

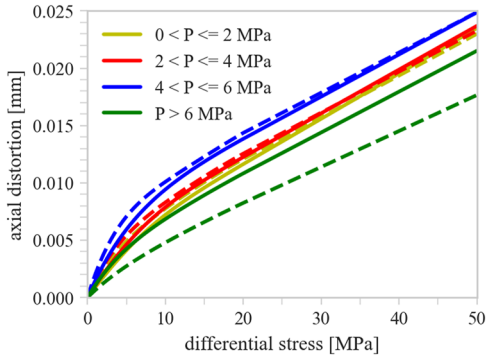

FIG. 5. Functions describing the axial displacement distortion for the different ranges of confining pressure. Equations describing these curves are summarized in Table I. Note that the loading (solid lines)–unloading (dashed lines) curves are averages of two repeated L-U cycles; hence, the L and U curves do not match up.

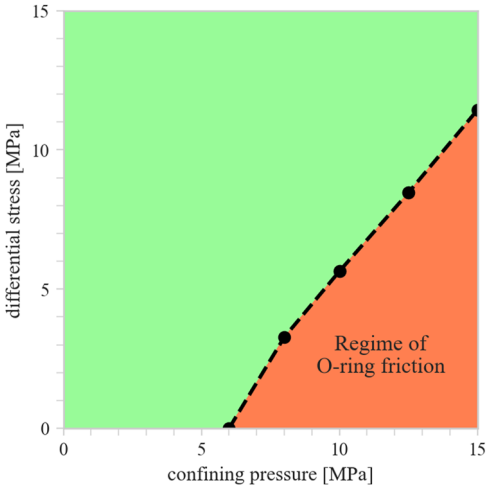

FIG. 6. Differential stress vs confining pressure plot showing the regimes where O-ring friction is an issue (orange) and where accurate measurements can be performed (green).

or cannot be performed accurately (Fig. 6). It can be concluded that only samples with a certain "minimum strength," i.e., given by the boundary between the two fields, can be used for testing. For example, to perform a test at 10 MPa confining pressure, the test sample should have an axial strength of well over 16 MPa to obtain sufficient data in the "measurable stress regime." As a result, it is possible that less competent rock types, such as poorly consolidated sandstones, soft shales, and weak chalks, will be less suitable in the current set-up.

III. CASE STUDIES

We completed three case studies to test the capabilities of the Harpers THMC flow bench under different testing conditions, as follows:

(a) we determined the permeability of a fractured granite sample and compared results with samples tested in another setup,

(b) we tested the mechanical response of a sandstone subjected to cyclic differential stress changes and,
(c) we performed reactive transport experiments on powdered granite over long time scales.

A. Permeability of fractured granite

In addition to the serial configuration described in Sec. II A, the setup can also be modified to support continuous fluid flow through multiple cells. Each cell can be isolated and tested either using a constant upstream pore pressure or a controlled flow rate. Pressure gradient Δp (Pa), flow rate Q ($m^3\ s^{-1}$), and temperature T (K) are continuously monitored. Together with the sample cross-sectional area A (m^2), sample length L (m) and fluid viscosity η (Pa s), the parameters allow for permeability calculation k_p (m^2) using Darcy's law and assuming steady state, laminar flow, and no sample storativity,

$$Q = \frac{A k_p}{L \eta} \Delta p. \quad (1)$$

Individual operation of the four cells allows for short- or long-term experiments that aim at investigating direct controls on sample permeability. Such controls can be (i) elastic or plastic deformation due to effective pressure or thermal expansion/shrinkage, (ii) long-term effects like creep, or (iii) reactive transport causing dissolution and precipitation reactions. Downstream of the sample, the fluid is collected in a burette at atmospheric pressure, allowing for the determination of flow rates as well as effluent sampling for the analysis of dissolved element concentrations.

To test the capability for permeability determination of the HFB, we injected deionized water into fractured Carnmenellis granite plugs and monitored permeability. The samples were obtained from a shallow mine in Cornwall, SW England, and are currently being investigated to understand fluid-rock interactions in a deep geothermal system targeted by the United Downs Deep Geothermal Project (Ledingham *et al.*, 2019). Furthermore, information about Cornish granites is provided in Simons *et al.* (2016). Following sample preparation with a short core drill (10 mm inner diameter), the plug was cut, and the surfaces were ground to be parallel. A tensile fracture was induced in a Brazilian test setup. During the first experiment, an upstream pressure of 0.5 MPa was applied, while the downstream pressure was against the atmosphere. Initially, confining pressure was increased to 20 MPa to tighten the steel sleeve against the sample. The sleeve would also tighten at lower confinement, but for the strong granite, a high stress was chosen to accelerate the process. Afterward, confining pressure and axial stress were controlled such that the sample was close to hydrostatic (isotropic) stress conditions. Thereby, we increased and then decreased the confining stress and axial stress in steps from 6, 10, 15, to 20 MPa three times [Fig. 7(a)]. During all these experiments, pore pressure remained constant. Over the three cycles completed, permeability decreased by more than two orders of magnitude, from 4.65×10^{-14} to 1.47×10^{-16} m^2. While the initial high permeability is likely related to flow around the sample, the decrease in permeability indicates sealing of the gap between the sample and steel layer and flow through the fracture in the plug. The comparison of a micro-CT scan prior to and post-permeability testing (both under ambient conditions using an EasyTom micro-CT scanner at Heriot-Watt University) clearly demonstrates that the confining steel has properly tightened against the sample and that no fluid bypass is expected (Fig. 8). It should be noted that the use of this thin steel layer allows for CT-scanning with minimal loss of radiation. The scan also shows the formation of wrinkles in the steel following a confining pressure increase that might act as additional flow paths to the fracture if not properly sealed. In this test, the sample was surrounded by PTFE tape that acted as a plastic seal closing such additional paths. The tape can be seen in the center of the wrinkles surrounding the rock. At the start of the second experiment, permeability slightly recovered to 1.03×10^{-15} m^2 as the sample was taken out of the cell for scanning [Fig. 7(b)]. Throughout the second experiment, permeability further decreased to 2.05×10^{-17} m^2.

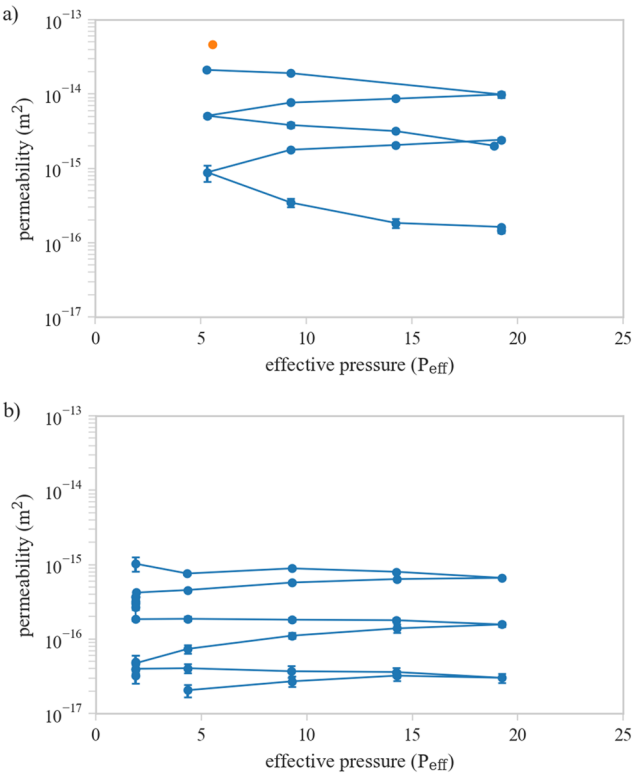

FIG. 7. Permeability development of a fractured Carnmenellis granite plug under effective pressure cycles. The sample was scanned using CT and then underwent the testing shown in (a). The orange datapoint indicates initial permeability before applying 20 MPa of confining stress initially to allow the steel sleeve of the sample holder to tighten against the sample. Following the first three cycles, the sample was CT-scanned again and then tested, as shown in (b).

Previous permeability measurements on a similar fractured Carnmenellis granite sample resulted in permeabilities around 7×10^{-16} m^2 at 19.5 MPa effective stress after two loading and unloading cycles of up to 30 MPa (not shown here). These were performed using samples of 1 in. in diameter (2.54 cm) and a length of 0.5 in. (1.27 cm) and making use of a permeameter with details provided previously (Forbes Inskip *et al.*, 2022; Phillips *et al.*, 2021). Permeability values using the "Harpers THMC Flow Bench" are

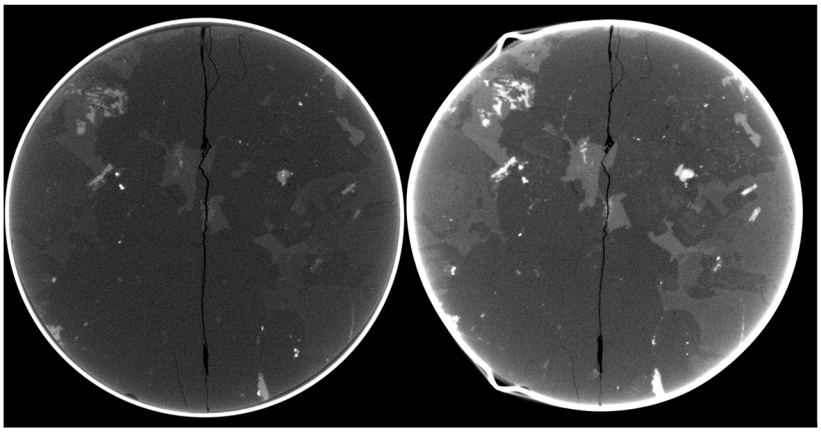

FIG. 8. CT scans of the fractured granite plug in the sample holder. Left: Scan before any loading; there is a small dark space between the sample and the steel sleeve (white rim). Right: Scan after effective pressure cycles shown in Fig. 7(a)—the sleeve has tightened around the sample, and small unconnected wrinkles have formed.

similar at 8.84×10^{-16} m^2 after the three effective stress cycles. In contrast to the permeameter data that show partial permeability recovery on effective pressure release, our tests show a continuous permeability decrease. A possible explanation is the steel sleeve surrounding the sample (the white rim in Fig. 8), which acts more ductile than the rubber sleeve used in the permeameter. This indicates that deformation is held in space instead of being allowed to recover.

B. Rock strength tests and cyclic differential stress tests

Cyclic loading is often encountered in various rock engineering applications. Especially for underground gas storage projects with frequent effective stress changes, cyclic loading can significantly affect the stability of the reservoir and its vicinity and even damage the rock near the borehole, impairing well performance (Hu *et al.*, 2018; Meng *et al.*, 2021). In this study, we performed strength tests and cyclic differential stress experiments using the "Harpers THMC Flow Bench" system at room temperature to explore the deformation characteristics and property changes of reservoir sandstone. The sample tested in this study was Castlegate sandstone from an outcrop in Utah, USA. The sandstone belongs to the Mesaverde Group, deposited in a fluvial environment and consisting mainly of quartz (about 90%) and minor feldspar, calcite, and clay (montmorillonite, kaolinite, and muscovite). The average grain size varies from 0.2 to 2.5 mm, with an average porosity of ~26% (Louis *et al.*, 2018; Rafieepour *et al.*, 2017). Because of its good physical properties, Castlegate sandstone is often used as a reservoir analog in laboratory tests (Plona and Cook, 1995; Rafieepour *et al.*, 2017). In this study, samples were drilled perpendicular to the bedding into plug samples with a diameter of 9 and 19–21 mm length. Both ends of the sample were ground flat and perpendicular to the sample axis using grinding paper to ensure uniform loading distribution during the tests. After drilling, samples were oven-dried at 60 °C for 48 h, wrapped in PTFE, and placed in sample holders for the following experiments.

We tested the strength of porous Castlegate sandstone at room temperature to determine the upper stress limit for the cyclic loading experiments. First, the syringe pump controller applied confining pressure to the cell at an average loading rate of 0.06 MPa/s up to 4.5 MPa. Next, the axial pressure was increased to be equal to the confining pressure to generate a hydrostatic (isotropic) stress state (differential stress = 0 MPa). Then, a syringe pump was used to inject deionized water into the sample holder with a loading rate of 0.05 MPa/s until the pore pressure reached 1 MPa. After the whole system was equilibrated for 5 min, the axial piston applied a compressive load at an average rate of 0.1 MPa/s until rock failure occurred. The system's axial pressure, confining pressure, and pore pressure were monitored by pressure sensors. The axial deformation of rock samples was monitored by LVDTs fitted to the axial pistons, and the time interval between data recording points was 12 s. The pump controller software was used to record the water flow rate at a frequency of 500 ms.

The experimental results are shown in Fig. 9. In general, the stress–strain curve consists of three stages. Before point A, the curve shows an upward concave shape, which may be related to the closure of micro-cracks existing in the Castlegate sandstone. Then, there is the AB stage (7–32 MPa), characterized by near-linear behavior, indicating that the sandstone exhibits apparent elastic behavior. The apparent Young's modulus of the sandstone in the elastic stage is 5.26 GPa. With further increases in axial stress, the rock finally enters the macroscopic yield stage (after B) and shows stress hardening (>32 MPa) until the peak strength of the rock is reached (59 MPa), and failure occurs, as indicated by a loss of strength. The cumulative strain of the whole process is about 1.8%. The rock strength obtained in this test (59 MPa under 4.5 MPa confining pressure) is greater than reported in previous studies [32 MPa under 6.89 MPa confining pressure in Jafarpour *et al.* (2012)]. In addition to our applied pore pressure that strengthens the rock, another potential reason is a lower porosity of ~19% in our samples, compared to ~26% porosity reported to be common in Castlegate sandstone (e.g., Chukwudozie *et al.*, 2012; Ingraham *et al.*, 2013; and Plona and Cook, 1995). Furthermore, the small size of our sample might affect

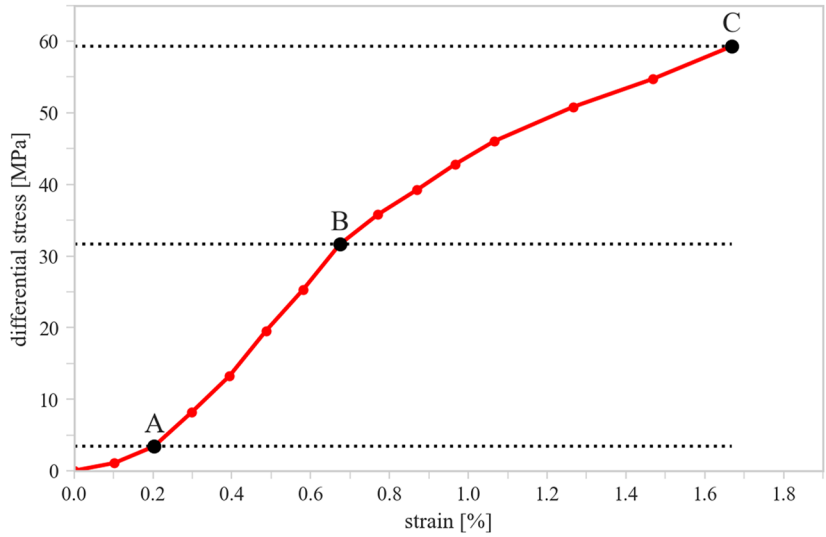

FIG. 9. Stress–strain curve of Castlegate sandstone at 4.5 MPa confining pressure and an axial loading rate of 0.1 MPa/s. Point A represents the entry into the elastic zone, and point B is the yield point, meaning that the deformation of Castlegate sandstone changes from the elastic to the plastic zone. Point C is the peak point at which Castlegate sandstone failure occurs.

strength as well. With a smaller sample size, the rock contains fewer microcracks, potentially resulting in higher strength (Han *et al.*, 2021; Hoek and Brown, 1997; and Mogi, 1962).

In the cyclic stress test, confining pressure was increased with an average loading rate of 0.06 MPa/s until 10.5 MPa. After the whole system was equilibrated for 5 min, axial stress was applied at an average loading rate of 0.1 MPa/s to achieve differential stresses of 10.5, 21, 31.5, and 42 MPa, respectively. The axial pressure of the system, confining pressure, and pore pressure were monitored by pressure sensors, and axial deformation was measured using LVDTs. In this study, confining and pore pressure were constant, and the axial stress was periodically loaded to oscillate the differential stress from 0 to 42 MPa for 5 times. The plot of stress vs strain of Castlegate sandstone under cyclic differential stress is shown in Fig. 10. Overall, at

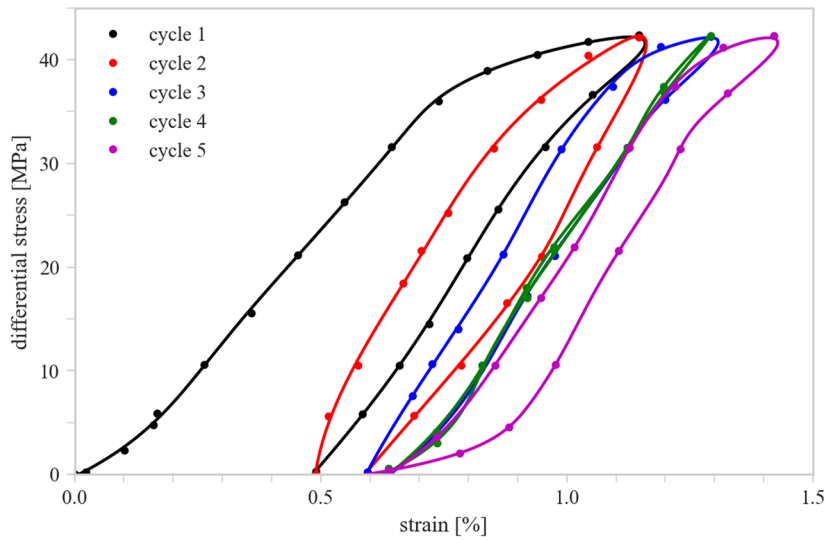

FIG. 10. Stress–strain curve of Castlegate sandstone under a cyclic differential stress test. After five cycles, the total axial strain in the rock was 1.4%, of which the inelastic strain was 0.64%, accounting for 47% of the total axial strain. The first stress cycle produced the largest inelastic strain of 0.48%. The inelastic strain leads to the loading curve and unloading curve not coinciding.

the early stage of the first loading (0.0% to 0.2% strain), the slope of the curve increases, showing a concave shape, followed by an elastic zone with a pronounced straight line (0.2% to 0.7% strain). The reason for the curve's behavior is that pre-existing microfractures in the rock are gradually closed with an increase in differential stress. The inflection point of the first cycle curve shifts more obviously to the right with increasing differential pressure. In addition, the curve has hysteretic cycles, which are formed when the stress applied to the rock exceeds the yield point or elastic limit. In this case, inelastic strain is generated, which leads to a hysteresis between the loading and unloading curves. After five axial stress cycles, the cumulative inelastic deformation is 0.64%, indicating that inelastic deformation plays an important role in the deformation of high porosity sandstone. The inelastic strain generated by the first stress cycle is the largest and then decreases gradually with progressing cycles.

The Castlegate sandstone was CT-scanned before and after loading to analyze deformation at the grain scale. The scanner operated at 150 kV and 500 μA. Each scan lasted 150 min and produced 4320 slices with a voxel size of 7.71 μm (see Fig. 11). The CT images show more porous areas within the sandstone before loading (e.g., the red square in Fig. 11). After cyclic loading, the sandstone underwent permanent compaction, and its pore space is reduced. Strain localization is observed near the top of the sample, as indicated by a reduction of porosity in the CT-slices in the top 7 mm of the sample length. According to previous studies, the micromechanisms of inelastic deformation in sandstone reservoirs in an upper crustal environment include (1) intergranular microcracking, (2) grain rearrangement and/or intergranular slip, (3) intra- and *trans*-granular microcracking, and (4) pressure dissolution (Pijnenburg *et al.*, 2018). In this test, mostly grain rearrangement and a small amount of intergranular microcracking under loading conditions contributed to the permanent deformation of the Castlegate sandstone.

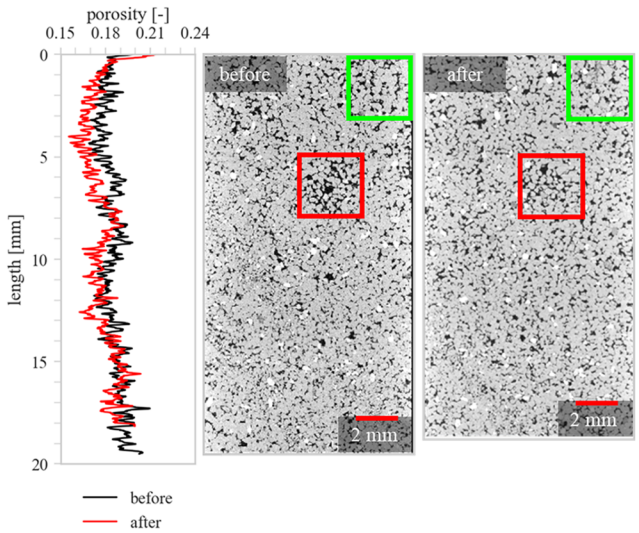

FIG. 11. Porosity distribution over the length of the Castlegate sandstone sample before and after cyclic loading (left) and vertical sections of the related CT scans (right). The red box shows pore space compaction due to inter-granular sliding under differential stress before and after cyclic loading, while the green box shows pore compaction due to intergranular microcracking.

C. Reactive-transport experiments

Fluids passing through or stored in fractured and porous rocks can significantly affect rock properties. In geothermal systems, the production of hot fluid and reinjection of cold fluid have the potential to significantly alter flow paths. This depends on the geochemical equilibrium that is affected by many factors, e.g., the temperature difference between rock and fluid, the composition of rock and fluid, the saturation state of the fluid, and the fluid flow rate. Our setup allows the injection of different complex brines into rock samples to analyze fluid-rock interaction and reactive transport.

As an example, we conducted a flow-through experiment on Carnmenellis granite powder (31 wt. % quartz, 20 wt. % plagioclase, 28 wt. % K-feldspar, 18 wt. % biotite + muscovite + illite, 1 wt. % kaolinite, 2 wt. % chlorite + smectite) that we filled into a sample holder. The powder was prepared by crushing, grinding, and sieving granite to a uniform grain size of <125 μm. Three grams of powder were placed between the two porous steel discs and pre-compressed manually within the holder. The test cell was heated to 80 °C, and axial stress and confining pressure were controlled to hold a constant value of 10 MPa. Initially, deionized water was injected into the system to displace all remaining air and create batch conditions (fluid saturated sample, no flow) for 48 h at a pore pressure of 0.5 MPa to give fluid and rock time to begin equilibration. Following the batch test, we flushed the system, reinjected deionized water with a constant flow rate of 2 μl/min, and collected effluents in a burette on the downstream side. Assuming a porosity of 30%, it will take ~4 h to replace the full pore volume. The powdered sample as well as low fluid flow rate were chosen to accelerate reactions by increasing fluid residence times and reactive surface area. We sampled the effluent from the burette over 37 days by taking one sample per day. Samples were then stored in a fridge until analysis.

Figure 12 shows the development of major cation concentrations (Si, Ca, Na, K, Al, Mg, and Li) in the effluent determined using inductively coupled plasma optical emission spectroscopy (ICP-OES). From an initial low concentration, most concentrations steeply increase and reach a maximum after 3–5 days. In the following, they tail off over the course of the experiment. Ca and Na seem to reach a constant value of ~0.1 mmol/l, which they hold until the end of the test. Si, K, and Li continue to decrease after 37 days, and Mg reaches a local minimum after 14 days, after which it increases continuously until the end of the test. In contrast to the other elements, the Al concentration was below the detection limit on day 0. It then reaches its maximum after the first day and, following a short decrease, reaches a second maximum after 14 days. Although the concentration behavior of the elements is relatively similar, the concentration levels differ significantly. Si shows the highest concentrations of around 1 mmol/l, while Ca, Na, and K only reach 0.2 mmol/l. In general, Al, Mg, and Li show the lowest concentrations, with a maximum of ~0.01 mmol/l.

As the purpose of the experiment was to leach elements from the rock by chemically reacting it with deionized water, the concentrations in the effluent hold information about which minerals were affected and how. Most concentrations slowly increase over

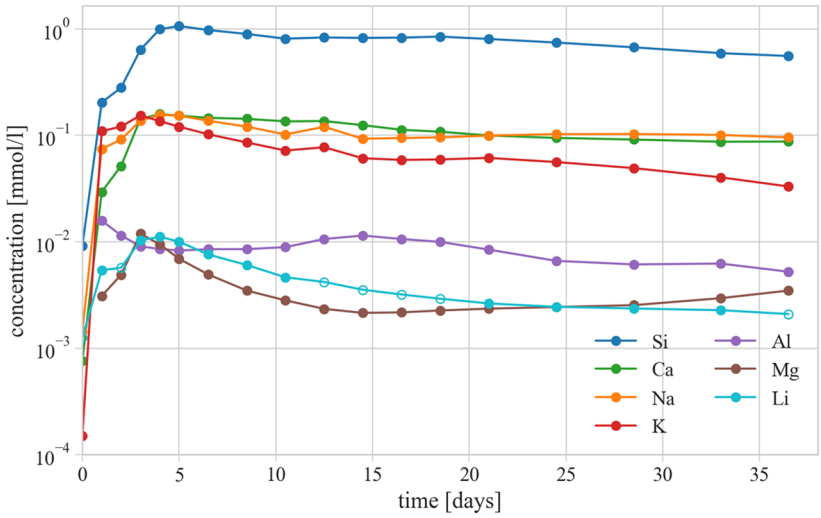

FIG. 12. Concentrations of major cations in the effluent of the leaching test over 37 days. The unfilled dots on the Li-concentration line represent low confidence data due to concentrations in diluted samples below the limit of quantification of the ICP-OES. However, using these data to calculate concentrations prior to dilution gives well-defined data following the trend.

the first three days, which is related to the relatively slow dissolution kinetics of silicate minerals [e.g., described in Palandri and Kharaka (2004)], showing maxima after 3–5 days. We interpret this as the dissolution of fines with a comparatively high surface area. Over time, these particles become less abundant, and concentrations begin to tail off toward constant values related to dissolution controlled by the flow rate, i.e., the availability of fresh fluid (Savage *et al.*, 1992). Si shows the highest concentration over the whole test duration. This is caused by silicate minerals dominating the mineralogy of the granite. Plagioclase and K-feldspar have been dissolved, as indicated by increasing aqueous Na, Ca, and K concentrations; their dissolution only partially contributes to the high Si concentration. In addition to the feldspars, quartz has started to dissolve, further increasing aqueous Si concentrations. Na and Ca were released in comparable amounts, indicating plagioclase dissolution. In addition, the dissolution of biotite is contributing to increasing aqueous K concentrations (in addition to K-Feldspar) and can explain the presence of Mg and Li in solution. However, Mg and Li levels are generally low (0.002–0.01 mmol/l) in comparison to the other elements (0.03–1.06 mmol/l), indicating limited dissolution of biotite.

IV. SUMMARY

In this work, we have introduced a new experimental device to measure the coupled thermo-hydro-chemical-mechanical properties of small rock samples (10 mm in diameter, 20 mm in length). The primary use of the device relates to geoenergy applications and is relevant for long-term testing of rock property changes associated with geological carbon and hydrogen storage, geothermal energy, or radioactive waste disposal. The "Harpers THMC Flow Bench" consists of four small triaxial cells that can be operated individually, allowing for long-term testing (frequently monitored, several months to a year). The cells can be heated up to 90 °C, and pore pressure, confining pressure, and axial pressure are individually controlled with a maximum pore and confining pressure of 20 MPa and a maximum axial load of 300 MPa. We can inject brines that are either saturated or unsaturated with gas at constant pore pressure or with continuous flow rates and analyze reactions by measuring effluent compositions and CT scanning samples before, during, and after experiments. A mixing autoclave can be added to the pressure cycle to allow the preparation of more complex fluids in equilibrium with a gas, which are then injected into the samples. Finally, LVDTs allow for testing of rock deformation while keeping in mind the small samples that are not necessarily representative of the rock itself.

The application of the flow bench is wide, and to demonstrate its capability, we performed initial tests to obtain granite fracture permeability by varying effective pressures as well as axial deformation of sandstone over differential stress cycles. We further show the results of a sandstone axial strength test and a chemical leaching experiment on granite powder using a constant flow of deionized water. The operational capacities and limitations of our setup are discussed by investigating leak rates, apparatus stiffness, O-ring friction, and the effect of the small sample size.

ACKNOWLEDGMENTS

We would like to acknowledge Jack Irvine and Hunter Scullion for their great help and effort to get the "Harpers THMC Flow Bench" operational. We would also like to mention that we are open to discuss collaborations with researchers who are interested in using the device.

AUTHOR DECLARATIONS

Conflict of Interest

The authors have no conflicts to disclose.

Author Contributions

Nick Harpers: Conceptualization (equal); Data curation (equal); Methodology (equal); Visualization (equal); Writing – original draft (equal); Writing – review & editing (equal). **Ming Wen**: Data curation (equal); Visualization (equal); Writing – original draft (equal). **Paul Miller**: Methodology (supporting); Supervision (supporting); Writing – review & editing (supporting). **Suzanne Hangx**: Data curation (equal); Visualization (supporting); Writing – original draft (equal); Writing – review & editing (supporting). **Andreas Busch**: Conceptualization (supporting); Supervision (equal); Writing – original draft (supporting); Writing – review & editing (supporting).

DATA AVAILABILITY

The data that support the findings of this study are available within the article.

REFERENCES

Boulin P. F., Bretonnier P., Gland N., and Lombard J. M., "Contribution of the steady state method to water permeability measurement in very low permeability porous media," Oil Gas Sci. Technol. **67**(3), 387–401 (2012).

Bui M., Adjiman C. S., Bardow A., Anthony E. J., Boston A., Brown S., Fennell P. S., Fuss S., Galindo A., and Hackett L. A., "Carbon capture and storage (CCS): The way forward," Energy Environ. Sci. **11**(5), 1062–1176 (2018).

Chapman, N. and Hooper, A., "The disposal of radioactive wastes underground," Proc. Geol. Assoc. **123**(1), 46–63 (2012).

Cheng C. and Milsch H., "Evolution of fracture aperture in quartz sandstone under hydrothermal conditions: Mechanical and chemical effects," Minerals **10**(8), 657 (2020).

Chukwudozie C. P., Tyagi M., Sears S. O., and White C. D., "Prediction of non-Darcy coefficients for inertial flows through the Castlegate sandstone using image-based modeling," Transp. Porous Media **95**(3), 563–580 (2012).

Drüppel, K., Stober, I., Grimmer, J. C., and Mertz-Kraus, R., "Experimental alteration of granitic rocks: Implications for the evolution of geothermal brines in the Upper Rhine Graben, Germany," Geothermics **88**, 101903 (2020).

Faoro, I., Elsworth, D., and Candela, T., "Evolution of the transport properties of fractures subject to thermally and mechanically activated mineral alteration and redistribution," Geofluids **16**(3), 396–407 (2016).

Faulkner D. R. and Armitage P. J., "The effect of tectonic environment on permeability development around faults and in the brittle crust," Earth Planet. Sci. Lett. **375**, 71–77 (2013).

Forbes Inskip N. D., Phillips T., Borisochev G., Esegbue O., Bisdom K., Meredith P. G., Callow B., and Busch A., "Linking fracture roughness and orientation to bedding: Impact on fluid flow," Earth Space Sci. Open Arch. (published online 2022).

Goldstein, B., Hiriart, G., Tester, J., Bertani, B., Bromley, R., Gutierrez-Negrin, L., Huenges, E., Ragnarsson, A., Mongillo, A., and Muraoka, H., "Great expectations for geothermal energy to 2100," paper presented at Proceedings 36th Workshop on Geothermal Reservoir Engineering, 2011.

Lima, M. G., Vogler, D., Querci, L., Madonna, C., Hattendorf, B., Saar, M. O., and Kong, X.-Z., "Thermally driven fracture aperture variation in naturally fractured granites," Geotherm. Energy **7**(1), 23 (2019).

Han, Q., Gao, Y., and Zhang, Y., "Experimental study of size effects on the deformation strength and failure characteristics of hard rocks under true triaxial compression," Adv. Civil Eng. **2021**, 6832775.

Hangx S. J. T. and Brantut N., "Micromechanics of high-pressure compaction in granular quartz aggregates," J. Geophys. Res.: Solid Earth **124**(7), 6560–6580, https://doi.org/10.1029/2018jb016494 (2019).

Hangx S. J. T., Spiers C. J., and Peach C. J., "Creep of simulated reservoir sands and coupled chemical-mechanical effects of CO_2 injection," J. Geophys. Res. **115**(B9), B09205, https://doi.org/10.1029/2009jb006939 (2010).

Hangx S. J. T., Bakker E., Bertier P., Nover G., and Busch A., "Chemical–mechanical coupling observed for depleted oil reservoirs subjected to long-term CO_2-exposure–A case study of the Werkendam natural CO_2 analogue field," Earth Planet. Sci. Lett. **428**, 230–242 (2015).

Heinemann, N. *et al.*, "Enabling large-scale hydrogen storage in porous media–The scientific challenges," Energy Environ. Sci. **14**(2), 853–864 (2021).

Hellmann, R., Renders, P. J., Gratier, J.-P., and Guiguet, R., "Experimental pressure solution compaction of chalk in aqueous solutions. Part 1. Deformation behavior and chemistry," *Water-Rock Interactions, Ore Deposits, and Environmental Geochemistry: A tribute to David A. Crerar* (The Geochemical Society, 2002), Vol. 7, pp. 129–152.

Hoek, E. and Brown, E. T., "Practical estimates of rock mass strength," Int. J. Rock Mech. Mining Sci. **34**(8), 1165–1186 (1997).

Hu C., Agostini F., Skoczylas F., Jeannin L., and Potier L., "Poromechanical properties of a sandstone under different stress states," Rock Mech. Rock Eng. **51**(12), 3699–3717 (2018).

Ingraham M. D., Issen K. A., and Holcomb D. J., "Response of Castlegate sandstone to true triaxial states of stress," J. Geophys. Res.: Solid Earth **118**(2), 536–552, https://doi.org/10.1002/jgrb.50084 (2013).

Jafarpour, M., Rahmati, H., Azadbakht, S., Nouri, A., Chan, D., and Vaziri, H., "Determination of mobilized strength properties of degrading sandstone," Soils Found. **52**(4), 658–667 (2012).

Kamali-Asl, A., Ghazanfari, E., Perdrial, N., and Bredice, N., "Experimental study of fracture response in granite specimens subjected to hydrothermal conditions relevant for enhanced geothermal systems," Geothermics **72**, 205–224 (2018).

Kim S. and Santamarina J. C., "Geometry-coupled reactive fluid transport at the fracture scale: Application to CO_2 geologic storage," Geofluids **16**(2), 329–341 (2016).

Krevor S. C. M., Pini R., Zuo L., and Benson S. M., "Relative permeability and trapping of CO_2 and water in sandstone rocks at reservoir conditions," Water Resour. Res. **48**(2), W02532, https://doi.org/10.1029/2011wr010859 (2012).

Ledingham, P., Cotton, L., and Law, R., "The united downs deep geothermal power project," paper presented at 44th Workshop on geothermal reservoir engineering, Stanford University, Stanford, California, 2019.

Lo Ré C., Kaszuba J. P., Moore J. N., and McPherson B. J., "Fluid–rock interactions in CO_2-saturated, granite-hosted geothermal systems: Implications for natural and engineered systems from geochemical experiments and models," Geochim. Cosmochim. Acta **141**, 160–178 (2014).

Louis, L., Henck, S., Honarpour, M., Araujo, E., and Bryant, D., "Experimental study on the hydromechanical behavior of a Gulf of Mexico reservoir sand analogue at *in situ* conditions of pressure and temperature," paper presented at 52nd U.S. Rock Mechanics/Geomechanics Symposium, 2018.

Meng M., Miska S., Yu M., and Ozbayoglu E. M., "Mechanical behavior of berea sandstone under cyclic loading: An application to dynamic loading of a Wellbore," SPE J. **26**(05), 2759–2779 (2021).

Mogi K., "The influence of the dimensions of specimens on the fracture strength of rocks: Comparison between the strength of rock specimens and that of the Earth's crust," Bull. Earthquake Res. Inst., Univ. Tokyo **40**(1), 175–185 (1962).

Nara Y., Kato M., Niri R., Kohno M., Sato T., Fukuda D., Sato T., and Takahashi M., "Permeability of granite including macro-fracture naturally filled with fine-grained minerals," Pure Appl. Geophys. **175**(3), 917–927 (2018).

Nermoen A., Korsnes R. I., Hiorth A., and Madland M. V., "Porosity and permeability development in compacting chalks during flooding of nonequilibrium brines: Insights from long-term experiment," J. Geophys. Res.: Solid Earth **120**(5), 2935–2960, https://doi.org/10.1002/2014jb011631 (2015).

Palandri, J. and Kharaka, Y., "A compilation of rate parameters of water-mineral interaction kinetics for application to geochemical modeling," Rep. 71, U.S. Geological Survey, 2004.

Phillips T., Bultreys T., Bisdom K., Kampman N., Offenwert S., Mascini A., Cnudde V., and Busch A., "A systematic investigation into the control of roughness on the flow properties of 3D-printed fractures," Water Resour. Res. **57**(4), ewrcr.25233, https://doi.org/10.1029/2020wr028671 (2021).

Pijnenburg R. P. J., Verberne B. A., Hangx S. J. T., and Spiers C. J., "Deformation behavior of sandstones from the seismogenic groningen gas field: Role of inelastic versus elastic mechanisms," J. Geophys. Res.: Solid Earth **123**(7), 5532–5558, https://doi.org/10.1029/2018jb015673 (2018).

Plona, T. J. and Cook, J. M., "Effects of stress cycles on static and dynamic Young's moduli in Castlegate sandstone," paper presented at the 35th U.S. Symposium on Rock Mechanics USRMS, 1995.

Rafieepour, S., Miska, S. Z., Ozbayoglu, E., Yu, M., Takach, N. E., Zhang, J., and Majidi, R., "Experimental study of reservoir stress path and hysteresis during depletion and injection under different deformational conditions," paper presented at 51st U.S. Rock Mechanics/Geomechanics Symposium, 2017.

Savage D., Bateman K., and Richards H. G., "Granite-water interactions in a flow-through experimental system with applications to the Hot Dry Rock geothermal system at Rosemanowes, Cornwall, U.K.," Appl. Geochem. **7**(3), 223–241 (1992).

Savage D., Bateman K., Milodowski A., and Hughes C., "An experimental evaluation of the reaction of granite with streamwater, seawater and NaCl solutions at 200°C," J. Volcanol. Geotherm. Res. **57**, 167–191 (1993).

Schimmel M. T. W., Hangx S. J. T., and Spiers C. J., "Impact of chemical environment on compaction creep of quartz sand and possible geomechanical applications," J. Geophys. Res.: Solid Earth **124**(6), 5584–5606, https://doi.org/10.1029/2019jb017464 (2019).

Simons B., Shail R. K., and Andersen J. C. Ø., "The petrogenesis of the Early Permian Variscan granites of the Cornubian Batholith: Lower plate post-collisional peraluminous magmatism in the Rhenohercynian Zone of SW England," Lithos **260**, 76–94 (2016).

Tarkowski, R., "Underground hydrogen storage: Characteristics and prospects," Renewable Sustainable Energy Rev. **105**, 86–94 (2019).

Yasuhara, H., "Thermal-hydraulic-mechanical-chemical couplings that define the evolution of flow and transport behavior in fractured rocks," in *ISRM International Symposium - 10th Asian Rock Mechanics Symposium* (International Society for Rock Mechanics and Rock Engineering, Singapore, 2018), p. 12.